Faraday Discussions

Explorations of the Nonheme High-Valent Iron-Oxo Landscape: Crystal Structure of a Synthetic High-valent Complex with an [FeIV2(mu-O)2] Diamond Core Relevant to the Chemistry of sMMOH

Journal:	*Faraday Discussions*
Manuscript ID	FD-ART-10-2021-000066.R1
Article Type:	Paper
Date Submitted by the Author:	21-Oct-2021
Complete List of Authors:	Rohde, Gregory; University of Minnesota Twin Cities Xue, Genqiang; University of Minnesota, Chemistry Que, Lawrence ; University of Minnesota, Chemistry

Explorations of the Nonheme High-Valent Iron-Oxo Landscape: Crystal Structure of a Synthetic Complex with an $[Fe^{IV}_2(\mu\text{-}O)_2]$ Diamond Core Relevant to the Chemistry of sMMOH

Gregory T. Rohde, Genqiang Xue, and Lawrence Que, Jr.

Department of Chemistry and Center for Metals in Biocatalysis, University of Minnesota, Minneapolis, Minnesota 55455, USA

Abstract

Methanotrophic bacteria utilize methane monooxygenase (MMO) to carry out the first step in metabolizing methane. The soluble enzymes employ a hydroxylase component (sMMOH) with a nonheme diiron active site that activates O_2 and generates a powerful oxidant capable of converting methane to methanol. It is proposed that the diiron(II) center in the reduced enzyme reacts with O_2 to generate a diferric-peroxo intermediate called **P** that then undergoes O–O cleavage to convert into a diiron(IV) derivative called **Q**, which carries out methane hydroxylation. Most (but not all) of the spectroscopic data of **Q** accumulated by various groups to date favor the presence of an $Fe^{IV}_2(\mu\text{-}O)_2$ unit with a diamond core. The Que lab has had a long-term interest in making synthetic analogs of iron enzyme intermediates. To this end, the first crystal structure of a complex with a $Fe^{III}Fe^{IV}(\mu\text{-}O)_2$ diamond core was reported in 1999, which exhibited an Fe•••Fe distance of 2.683(1) Å. Now more than 20 years later, a complex with an $Fe^{IV}_2(\mu\text{-}O)_2$ diamond core has been synthesized in sufficient purity to allow diffraction-quality crystals to be grown. Its crystal structure has been solved, revealing an Fe•••Fe distance of 2.711(4) Å for comparison with structural data for related complexes with lower iron oxidation states.

Nature often uses iron centers to activate dioxygen and generate high-valent oxidants that cleave the strong C–H bonds of substrates and carry out substrate functionalization into a range of products.[1] Of particular interest for this article is the soluble methane monooxygenase (sMMO), which catalyzes the hydroxylation of methane to methanol in methanotrophic bacteria.[2] Methane has a C–H bond of 104 kcal mol^{-1}, representing the strongest bond found among aliphatic hydrocarbons. The hydroxylase component of the sMMO enzyme, sMMOH, belongs to a family of diiron enzymes in which two His and four Asp/Glu residues are bound to the diiron active site.[1,2] Figure 1 shows the recently reported high-resolution XFEL structure of the sMMOH from *Methylosinus trichosporium* OB3b that is bound to its regulatory component.[2c] The diferrous enzyme uses two of the four active-site carboxylates as bridging ligands to the diiron(II) unit, one as a monodentate bridge and the other as a 1,3-bridge (Figure 1A), the diferric form has the two iron(III) centers bridged by two hydroxo groups together with the 1,3-bound carboxylate found in the diferrous form (Figure 1B).

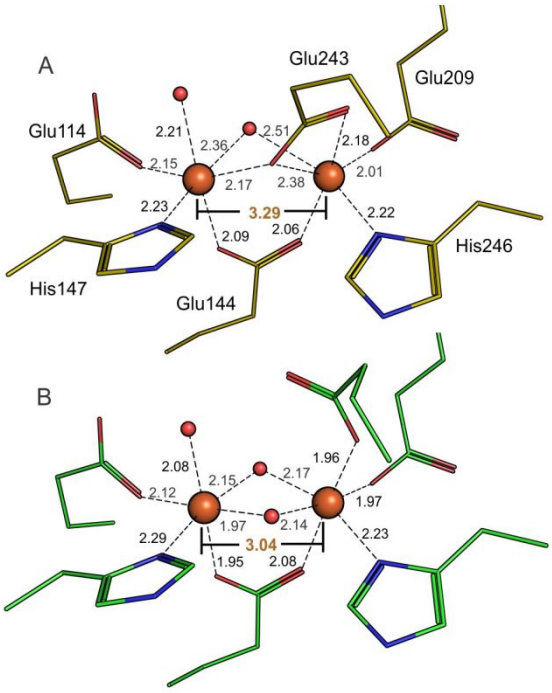

Figure 1. Diiron active sites of diferrous (A) and diferric (B) forms of sMMOH from *Methylosinus trichosporium* OB3b based on the high-resolution XFEL studies of the enzyme bound to its regulatory component.[2c]

The high-valent diiron oxidant for methane hydroxylation generated at the sMMOH active site is formed in two key steps (Scheme 1).[3] In step 1, O_2 binding to the diferrous enzyme generates an O_2-adduct called **P** or H_{peroxo}, which is best described as a (μ-1,2-peroxo)diferric intermediate commonly observed in model complexes.[4,5] In step 2, the O–O single bond of **P** is cleaved with the help of a proton to generate the diiron(IV) oxidant **Q** that is capable of cleaving the 104-kcal•mol^{-1} C–H bond of methane. Both intermediates have been observed and characterized by Mössbauer spectroscopy. Intermediates **P** obtained from both *M. capsulatus* and *M. trichosporium* enzymes exhibit isomer shifts (δ) of 0.66-0.67 mm•s^{-1} and quadrupole splittings (ΔE_Q) of 1.51 mm•s^{-1}, values strongly indicative of high-spin ferric centers. On the other hand, the intermediate **Q** derived from *M. trichosporium* sMMOH displays a single quadrupole doublet with an isomer shift (δ) of 0.17 mm•s^{-1} and a quadrupole splitting (ΔE_Q) of 0.53 mm•s^{-1}, while that from *M. capsulatus* gives rise to two distinct quadrupole doublets of equal intensity with δ values of 0.21 and 0.14 mm•s^{-1} and ΔE_Q values of 0.68 and 0.55 mm•s^{-1}, respectively. These observed isomer shifts clearly reflect the formation of Fe(IV) centers in intermediate **Q**. Lastly, the decay of **P** leading the formation of sMMOH-**Q** has been shown to be pH dependent, with O–O bond cleavage found to be facilitated by one or more protons.[1b]

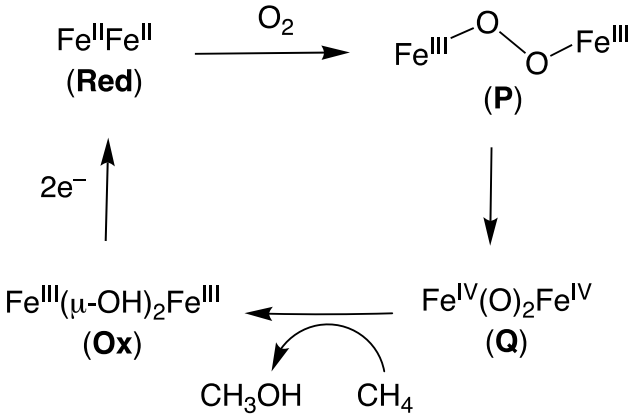

Scheme 1. Steps proposed in the activation of O_2 at the diiron active site of sMMOH and the subsequent hydroxylation of methane. Both the formation of intermediate **P** from diferrous sMMOH and the reaction of methane with intermediate **Q** leading to the release of products actually involve several steps, which have been characterized in kinetic and spectroscopic studies of the enzyme.[3]

Initial efforts to gain insight into the nature of the high-valent diiron center in sMMOH using X-ray absorption spectroscopy showed evidence for a 2.46-Å Fe•••Fe distance in intermediate Q,[6a] suggesting the possibility of an $Fe^{IV}_2(\mu\text{-}O)_2$ diamond core. However, subsequent efforts in characterizing synthetic diiron complexes with $Fe_2(\mu\text{-}O)_2$ diamond cores revealed Fe•••Fe distances that fall within a range of 2.6-2.8 Å,[7b,7e-7h] which are longer than the 2.46-Å distance deduced for sMMOH-**Q**.[6a] More recent results from DeBeer *et al.* using high-energy resolution fluorescence detected extended X-ray absorption fine structure methodology found no evidence for such a short Fe•••Fe distance, but instead supported a longer Fe•••Fe distance of 3.4 Å, which could come about by isomerization of the diamond core into an open core with a terminal Fe=O unit (Scheme 2).[6b,6c] On the other hand, Lipscomb and Proshlyakov applied resonance Raman techniques to identify a peak at 690 cm^{-1} ($\Delta\nu^{18}O$ = -36 cm^{-1})[6d] that falls in the range of values associated with a $M_2(\mu\text{-}O)_2$ core vibration in synthetic complexes.[7a] This apparent disagreement between EXAFS- and resonance Raman-based interpretations has not yet been resolved. However, recent studies of sMMOH-**Q** just reported by Solomon and coworkers employing nuclear resonance vibrational spectroscopy strongly favor a closed-core description for this intriguing intermediate.[6e]

Synthetic complexes that mimic the O_2-derived intermediates formed in the sMMOH active site have also contributed to our understanding of the enzyme active site. Numerous examples of diferric-peroxo complexes have been characterized over the last three decades, with crystal structures available for five of these as well as a wealth of structural and spectroscopic data for comparison.[4,5] Notably, there are three cases in which the peroxo species has been shown to undergo 1-electron reductive cleavage of the O–O bond to generate an $Fe^{III}Fe^{IV}$ species stable enough to be characterized spectroscopically.[4d,e,f] However, the corresponding conversion of a synthetic diferric-peroxo species into the isoelectronic bis(μ-oxo)diiron(IV) species has been more difficult to accomplish (Scheme 1). Indeed, only recently has such a transformation been reported where $[Fe^{IV}_2(\mu\text{-}O)_2(Me_3NTB)_2]^{4+}$ (Me_3NTB = tris((1-methyl-1H-benzo[d]imidazol-2-yl)-methyl)amine) was formed in ~35% yield upon addition of the highly Lewis acidic $Sc(OTf)_3$ to $[Fe^{III}_2(\mu\text{-}O)(\mu\text{-}1,2\text{-}O_2)(Me_3NTB)_2]^{2+}$.[7j] In this paper, we describe another example of the

synthesis of such a putative analog for sMMOH-**Q**, which was obtained in 85% yield from the reaction of $[Fe^{III}_2(\mu\text{-}OH)_2(TPA^*)_2]^{4+}$ (TPA* = tris(3,5-dimethyl-4-methoxypyridyl-2-methyl)amine) with stoichiometric H_2O_2. The high yield of the $[Fe^{IV}_2(\mu\text{-}O)_2(TPA^*)_2]^{4+}$ complex has allowed diffraction-quality crystals to be obtained and the first crystal structure of a synthetic complex with an $Fe^{IV}_2(\mu\text{-}O)_2$ core to be reported herein.

Results and Discussion

One-step formation of a complex with a bis(μ-oxo)diiron(IV) core

Previously, we reported that the $[Fe^{IV}_2(\mu\text{-}O)_2(TPA^*)_2]^{4+}$ complex (**4A**) could be prepared by two different routes, a) by the nearly quantitative bulk electrolytic oxidation of the green $[Fe^{III}Fe^{IV}(\mu\text{-}O)_2(TPA^*)_2]^{3+}$ complex (**3A**) to the red **4A** complex[7e] and b) by the reaction of H_2O_2 with the $[Fe^{III}_2(\mu\text{-}O)(\mu\text{-}OH)(TPA^*)_2]^{3+}$ precursor (**1A**) to generate a diiron(IV) complex with an open $[(O)Fe^{IV}(\mu\text{-}O)Fe^{IV}(OH)]^{3+}$ core (**OC** $Fe^{IV}Fe^{IV}$) followed by protonation with 1 equiv. $HClO_4$ to afford **4A** in about 40% yield (Scheme 2).[7e] Despite many attempts, neither synthetic procedure afforded crystals of **4A**.

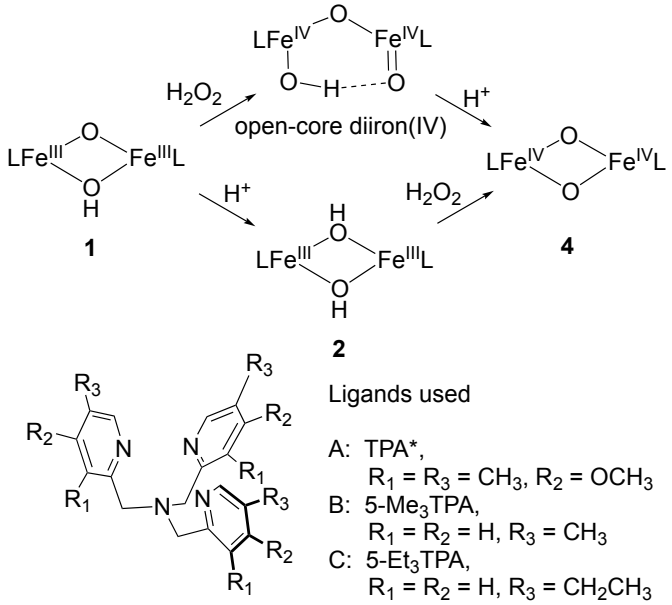

Scheme 2. Two pathways for the conversion of $[Fe^{III}_2(\mu\text{-}O)(\mu\text{-}OH)(L)_2]^{3+}$ (**1A**) to $[Fe^{IV}_2(\mu\text{-}O)_2(L)_2]^{4+}$ (**4A**) depending on the order of addition of H_2O_2 and H^+. Adding H_2O_2 to **1A** first generates $[(L)Fe^{IV}(\mu\text{-}O)(\mu\text{-}OH\bullet\bullet\bullet O)\text{-}Fe^{IV}(L)]^{3+}$, an open-core diiron(IV) species, and then converts into **4A** upon protonation in 40% yield. On the other hand, reversing the order by introducing H^+ first to form **2A** and then adding H_2O_2 increases the yield of **4** to 85%.

We then explored the possibility of reversing the order of addition for H_2O_2 and $HClO_4$ (Scheme 2) and indeed obtained a much higher yield of **4A**, as indicated by the higher intensity of the characteristic 875-nm band of **4A**. The addition of 1 equiv. strong acid to **1A** generated its conjugate acid **2A (**$[Fe^{III}_2(\mu\text{-}OH)_2(L)_2]^{4+}$), which could be isolated and characterized (*vide infra*). Upon treatment with 1 equiv. 70% H_2O_2 at -40°C, **2A** was converted into **4A** in 85% yield (Figure 2 top). The characteristic features of **4A** at 485 and 875 nm achieved maximal intensity in less than 30 seconds. Thus this method represents the best strategy for obtaining **4A** in high yield and purity.

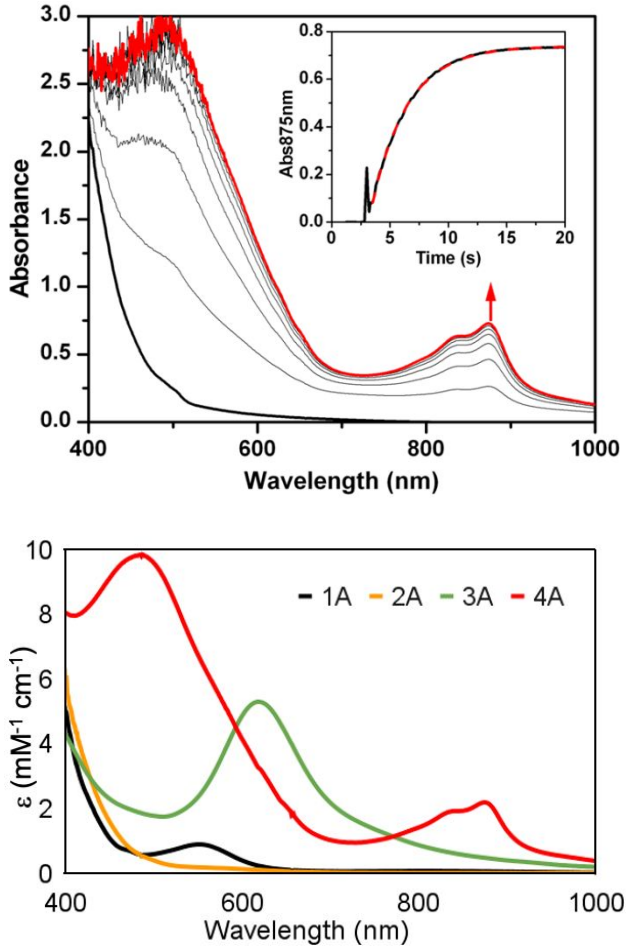

Figure 2: A (top): Formation of **4A** from the reaction of 0.3 mM **2A** in MeCN with 1 equiv. 70% H_2O_2 at -40°C in 85% yield as determined by UV-Vis spectroscopy. B (bottom): Comparison of electronic spectra of **1A**, **2A**, **3A**, and **4A**, showing the significantly more intense visible/near IR features of the higher-valent complexes.

Structural Characterization of 1A and 2A

Of the TPA* complexes discussed in this paper, only the crystal structure of **1A** had been previously reported.[7f] However, due to crystallographic symmetry averaging, an effective inversion center was found in the crystal, so the Fe-*μ*-O and Fe-*μ*-OH bonds were disordered over the two positions. EXAFS methods were then applied to determine Fe-*μ*-O and Fe-*μ*-OH bond distances with good accuracy, provided that there was a sufficient difference in their bond lengths relative to the resolution of the measurement. EXAFS data were then collected on a crystalline sample of **1A** with a unit cell that matched the published parameters [7f] and was diluted with boron nitride; the data thus obtained at 20 K had a resolution of 0.12 Å. The EXAFS data displayed in Figure 3A together with the best fit listed in Tables 1 and S1 show excellent agreement between the XAS and XRD data, with respective Fe–N_{ave} distances of 2.14 Å and 2.15(2) Å and respective Fe•••Fe distances of 2.80 and 2.7920(9) Å. Importantly, the two Fe-*μ*-O distances at 1.80 Å and 1.97 Å could be resolved and respectively assigned to the Fe-*μ*-O and Fe-*μ*-OH distances based on previously characterized oxo- and hydroxo-bridged diferric complexes.[7c,d,e,f] The unsymmetric Fe^{III}_2(μ-O)(μ-OH) core of **1A** is thus accurately modeled by the EXAFS analysis.

Table 1: EXAFS analysis of complexes having Fe_2(μ-O(H))$_2$ diamond cores that are supported by the TPA* ligand.

	Fe–N			Fe–O			Fe•••C			Fe•••Fe		
Complex	N	R	σ^2	N	R	σ^2	N	R	σ^2	N	R	σ^2
1A	4	2.14	3.3	1 1	1.80 1.97	1.5 4.7	6	3.00	1.3	1	2.80	3.8
2A *(solid)*	4	2.10	2.3	2	1.91	5.4	4	2.95	-2.9	1	3.04	-1.2
2A *(soln)*	5	2.12	4.3	1	1.79	0.0	8	3.03	2.6	1 4[m]	3.42 3.57	0.1 0.8
3A	4	1.96	8.9	2	1.75	7.3	6 4	2.92 2.77	1.7 0.8	1	2.57	2.4

1A = $[Fe^{III}_2$(μ-O)(μ-OH)(TPA*)$_2]^{3+}$, **2A** = $[Fe^{III}_2$(μ-OH)$_2$(TPA*)$_2]^{4+}$, **3A** = $[Fe^{III}Fe^{IV}$(μ-O)$_2$(TPA*)$_2]^{3+}$. N = number of scatterers; R = scatterer distance listed in Å.; σ^2 = mean-squared deviation in units of 10^{-3} Å^2. The superscript [m] used in one of the fits for **2A** indicates the inclusion of a multiple scattering pathway for the nearly linear Fe–O–Fe unit. See SI for complete EXAFS analysis and methods.

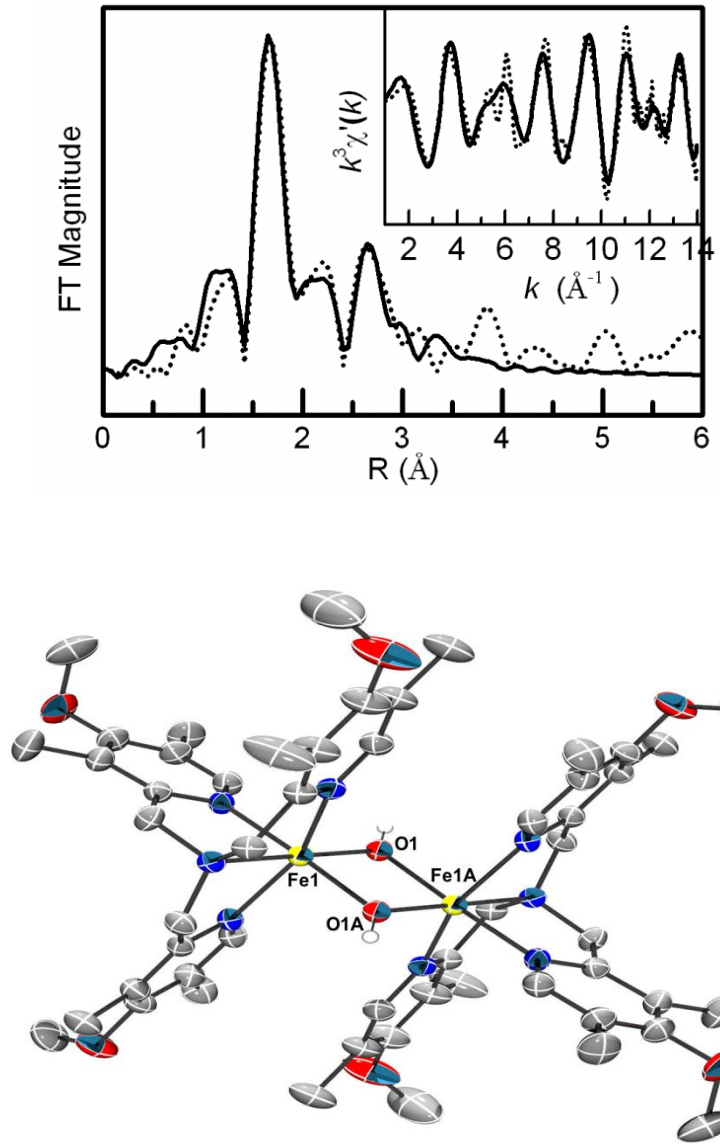

Figure 3. A (top panel) Fourier-transformed Fe K-edge EXAFS data for $[Fe^{III}_2(\mu\text{-}O)(\mu\text{-}OH)(TPA^*)_2]^{3+}$ (**1A**) obtained on a 1:13 **1A**:boron nitride solid mixture at 20 K. *Inset*: $k^3\chi'(k)$ data. Fourier transform range 1-14 Å^{-1}; experimental data (dotted line) and the best fit (solid line) consisting of 1 O at 1.80 Å, 1 O at 1.97 Å, 4 N at 2.14 Å, 1 Fe at 2.80 Å, and 6 C at 3.00 Å. B (bottom panel) Thermal ellipsoid plot of 2A ($[Fe^{III}_2(\mu\text{-}OH)_2(TPA^*)_2]^{4+}$) showing 50% probability ellipsoids. Non-oxygen bound hydrogen atoms, perchlorate counterions and acetonitrile and water solvent molecules were removed for clarity. Colors of atoms: carbon, gray; oxygen, red; nitrogen, blue; iron; orange, hydrogen, green. Selected bond distances (Å) and angles (°): Fe1–O1, 1.926(2); Fe1–O1A, 1.995(2); Fe1•••Fe1A, 3.0224(7); Fe–N_{ave}, 2.114; Fe1–O1–Fe1A, 100.86(11). See Table 2 for a comparison with other diiron complexes with $Fe_2(\mu\text{-}O)_2$ diamond cores.

Complex **2A** was synthesized from the reaction of stoichiometric amounts of $Fe(ClO_4)_3$, TPA*, and NaOH in methanol/water at room temperature. Suitable crystals of **2A** for X-ray diffraction were grown by the slow diffusion of diethyl ether into an acetonitrile solution of microcrystalline **2A**. The diamond core structure of **2A** (Figure 3B, Table 2) is similar to those of **1A** and other (*μ*-hydroxo)(*μ*-oxo)diiron(III) complexes supported by similar tripodal ligands.[7d,e,f] The diamond core of **2A** is in fact better described as a rhomb where the hydroxo bridge is bound unsymmetrically, with Fe–*μ*-OH bond distances of 1.926(2) and 1.995(2) Å (Table 2). The latter falls within the range of previously published bridging Fe-*μ*-OH bond distances [7d,e,f] and very close to the Fe–*μ*-OH bond distance determined for the Fe-*μ*-OH bond in **1A** by EXAFS (Table 1). The other Fe–*μ*-OH bond distance is on the short end of the range, but nevertheless still significantly longer than the Fe-*μ*-O bond of **1A** determined by EXAFS (Table 1). The asymmetry of the Fe–OH–Fe unit reflects the nature of the different ligands *trans* to the hydroxo bridge in the dinuclear unit, namely a tertiary amine on one Fe and a pyridine on the other, which form Fe–N bonds of different lengths (Table 2). The average $Fe–N_{amine}$ and $Fe–N_{pyr}$ bond lengths of **2A** are shorter by about 0.03 Å and 0.05 Å, respectively, than those of **1A**, reflecting the lower basicity of the two hydroxo ligands of **2A** compared to the oxo and hydroxo ligands for **1A** (Table 2), making the iron centers of **2A** more Lewis acidic than those of **1A**.[7f] Interestingly, the Fe•••Fe distance of **2A** is 3.0224(10) Å, the longest distance found in this series of diiron diamond core complexes (Table 2).

Table 2. Select bond distances and angles for complexes with $Fe_2(\mu\text{-}O)_2$ diamond cores based on data from XRD studies with EXAFS-derived values listed in italics within square brackets.

Complex*	**0C**	**1A**	**2A**[a,b]	**3B**	**3A**	**4A**[a]	**4D**
Diiron core (L =)	$Fe^{III}_2(\mu\text{-}O)_2$ 6-Me_3TPA	$Fe^{III}_2(\mu\text{-}O)(\mu\text{-}OH)$ TPA*	$Fe^{III}_2(\mu\text{-}OH)_2$ TPA*	$Fe^{3.5}_2(\mu\text{-}O)_2$ 5-Et_3TPA	$Fe^{3.5}_2(\mu\text{-}O)_2$ TPA*	$Fe^{IV}_2(\mu\text{-}O)_2$ TPA*	$Fe^{IV}_2(\mu\text{-}O)_2$ Me_3NTB
Fe1–O1	1.842(5)	1.883(3)[c] [*1.80*]	1.926(2) [*1.91*]	1.805(3) [*1.82*]	**1.781(4)** **[*1.75*]**	**1.790(6)** **[*1.77*]**	[*1.78*]
Fe1–O1A	1.917(4)	1.934(2)[c] [*1.97*]	1.995(2)	1.860(3)	1.827(5)	1.809(8)	
Fe1–N_{amine}	2.192(5)	2.183(3)	2.150(3)	2.049(3)	2.012(6)	1.992(7)	
ave Fe–N_{py}	2.258(12)[d]	2.144(9)[d]	2.103(14)[d]	2.018(13)[d]	1.989(5)[d]	1.967(8)[d]	
ave Fe–N	2.242(34)[d]	2.154(21)[d] [*2.14*]	2.114(26)[d] [2.10]	2.026(19)[d] [*2.00*]	1.995(13)[d] [*1.96*]	1.973(14)[d] [*1.97*]	[*1.97*]
Fe1•••Fe1A	2.714(1)	2.7920(9) [*2.80*]	3.0224(7) [3.04]	2.683(1) [*2.61*]	**2.596(1)** **[*2.57*]**	**2.711(4)** **[*2.73*]**	[*2.70*]
Fe1–O1–Fe1A	92.4(2))	94.0(1)	100.86(11)	94.1(1)	92.0(2)	97.8(4)	
O1–Fe1–O1A	87.6(2	85.99(11)	79.14(11)	85.9(1)	88.0(2)	82.2(3)	
λ_{max} (ε_M)	470 (560) 760 (80)	550 (~900)		616 (6200)	620 (~6000)	485 (9800) 875 (2200)	600 (9000)
Raman $\nu(Fe_2O_2)$ (^{18}O shift)	692 (-32)	770 (-42)		666 (-35)	661[e] (-33)	674 (-30)	653 (-30) 528 (-17)
XRD Refs	7b	7f	This work	7d	This work	This work	—
Spectroscopic Data	7e	This work, 7f	This work	7c,d;8b,c	7g	7g	7j
Counter Anion	ClO_4^-	ClO_4^-	ClO_4^-	ClO_4^-	ClO_4^-	ClO_4^-	Triflate

*Shaded columns in the table highlight complexes with $[Fe^{III}_2(\mu\text{-}O)_2]$ cores, with complexes **0**, **1**, and **2** having 0, 1, and 2 additional protons, respectively. [a] Average of two molecules in the asymmetric unit. [b] An isomer of **2A** is observed in MeCN and shown to have an open $(H_2O)Fe^{III}$–O–$Fe^{III}(OH_2)$ core by EXAFS with these distances: Fe–μ-O, 1.79 Å; Fe–N_{ave}, 2.12 Å; Fe1•••Fe1A, 3.42 Å (see Table 1). Its rRaman spectrum shows two ^{18}O-sensitive vibrations at 835(-40) cm^{-1} and 463(-8) cm^{-1}; see Scheme 3. [c] From ref 7f; the oxo and hydroxo ligands cannot be resolved in XRD due to disorder over an inversion center. [d] Standard deviation reported from the average of Fe–N distances specified from the crystal structures. [e] Observed as a Fermi doublet.

The solution structure of **2A** in MeCN has been investigated by EXAFS to gain insight into the nature of the diferric complex in solution, as some synthetic nonheme diferric complexes can exist either as a diamond core or an open core (Scheme 3). X-ray crystallography of **1A** by Do *et al.* showed it to have a closed core with dimensions comparable to related nonheme diiron complexes.[7d,e,g] However, the diiron core of **1A** has been observed to open in the presence of H_2O in MeCN solution,[7f] but the active form responsible for activating H_2O_2 is still likely to be the closed core form. Thus understanding the core isomerization equilibrium is important for understanding the mechanism of H_2O_2 activation by these complexes. Therefore the solution geometry of **2A** has been investigated with several techniques in order to elucidate the structure of the diferric starting material.

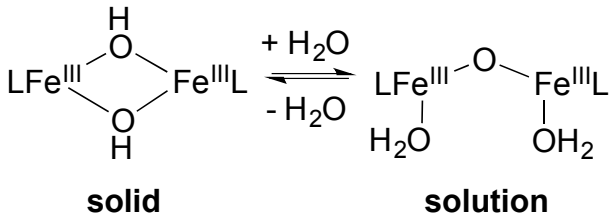

Scheme 3. Distinct structures of **2A** in the solid state and in MeCN solution, resulting in an increase in the Fe•••Fe distance from 3.04 Å in the solid state to 3.42 Å in MeCN solution. Acetonitrile may replace the bound water molecules shown above.

EXAFS analysis of **2A** in the solid-state and as a frozen solution sample shows that the different sample states result in dramatic changes in diiron core dimensions. The Fourier transform (*R*' space) of the Fe K-edge EXAFS data of microcrystalline **2A** diluted with BN (1:20) exhibits several prominent peaks (Figure 4 top; Tables S2 & S3). Of note is the feature at R+Δ ~ 2.6 Å with an intensity comparable to those of the first shell at R+Δ < 2 Å; this feature is assigned to the other Fe in an $Fe^{III}_2(OH)_2$ diamond core with an Fe•••Fe distance of 3.04 Å.[7c,e] In addition, there are two O scatterers at 1.91 Å that arise from the bridging hydroxo ligands, consistent with its crystal structure (*vide infra*).

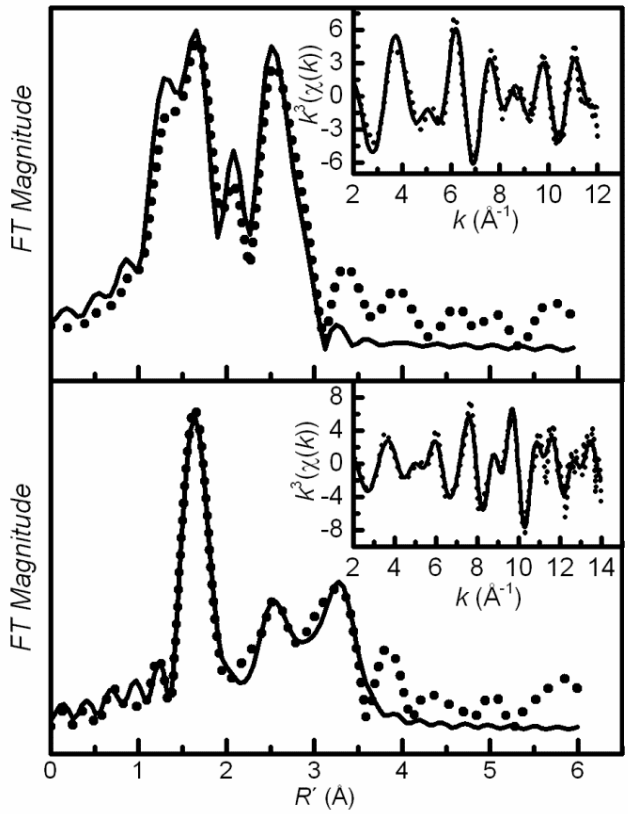

Figure 4. Top: EXAFS data (dots) for microcrystalline **2A** diluted 1:20 in BN with the best fit (solid line) consisting of four shells at 1.91 Å (2 O scatterers), 2.10 Å (4 N scatterers), 2.95 Å (6 C scatterers) and 3.04 Å (1 Fe scatterer). Bottom: EXAFS data for a 5-mM solution of **2A** in MeCN with the best fit consisting of five shells at 1.79 Å (1 O scatterer), 2.12 Å (5 N/O scatterers), 3.03 Å (6 C scatterers), 3.42 Å (1 Fe scatterer) and one 3.57-Å multiple scattering pathway modeled with a Fe–O–Fe unit. In the insets are Fourier transforms of the unfiltered EXAFS experimental data for **2A** in *k*-space (dotted line) and the best fits (solid line).

On the other hand, the EXAFS spectrum for a 5-mM frozen solution of **2A** in anhydrous acetonitrile (Figure 4 bottom) differs dramatically from that obtained for the solid-state sample, showing a change in the diiron core structure upon dissolution. The prominent feature at R+Δ ~ 2.6 Å assigned to the Fe scatterer in the microcrystalline sample is absent and replaced by a less intense feature around 3.3 Å associated with a heavy atom scatterer that is at a longer distance and in a more flexible environment than in the crystalline sample (Table 2). The best fit for the data requires 1 O scatterer at 1.79 Å and 1 Fe scatterer at 3.42 Å, which together suggest the presence of a nearly linear

Fe–O–Fe unit with an Fe–O–Fe angle of 146°. Furthermore, an acceptable fit requires the inclusion of a 3.569-Å multiple scattering pathway via the nearly linear Fe–O–Fe unit commonly found in the crystal structures of oxo-bridged diferric complexes with similar TPA-based ligands.[7d,e,g] Thus the geometry of **2A** in solution is best described as a nearly linear open core in solution as opposed to the diamond core form strongly favored in the solid state; therefore it is designated as **2A'**. On the other hand, we note that the diamond core found in the crystal structure of **1A** is conserved in solutions with low H_2O concentrations but converts to an open core structure at higher H_2O concentrations,[7d] consistent with the lower Lewis acidity of its iron(III) centers.

Resonance Raman studies on a frozen solution of **2A'** provide additional support for the structural conclusions derived from EXAFS analysis. The ν_{sym}(Fe–O–Fe) and ν_{asym}(Fe–O–Fe) stretching frequencies of (μ-oxo)diiron(III) complexes have been found to correlate well with the Fe–O–Fe model.[8a,b] Indeed, **2A'** exhibits a feature at 835 cm^{-1} in frozen MeCN solution that can be assigned to the ν_{asym}(Fe–O–Fe) mode and shifts to 795 cm^{-1} upon ^{18}O labeling of the oxo bridge (Figure 5). The observed downshift of ~40 cm^{-1} is in agreement with the expected shift calculated for a Fe–O diatomic oscillator according to Hooke's Law. A second feature is observed at 463 cm^{-1}, which downshifts by 8 cm^{-1} with ^{18}O-substitution and is consistent with its assignment to the ν_{sym}(Fe–O–Fe) mode (Figure 6). Taken together, both vibrations indicate an open core structure based on previous studies with an Fe–O–Fe angle between 140-150°, which closely matches the angle calculated from the EXAFS scatterer distances.[7b,8] The EXAFS and resonance Raman experiments thus strongly support the open core formulation for **2A'** (Scheme 3). An H-bonded water molecule found in the unit cell of **2A** is the likely source of the second aqua ligand. While EXAFS cannot conclusively rule out MeCN binding instead of the aqua ligand, water is found bound to both Fe centers in other published structures of related complexes recrystallized from MeCN.[7g]

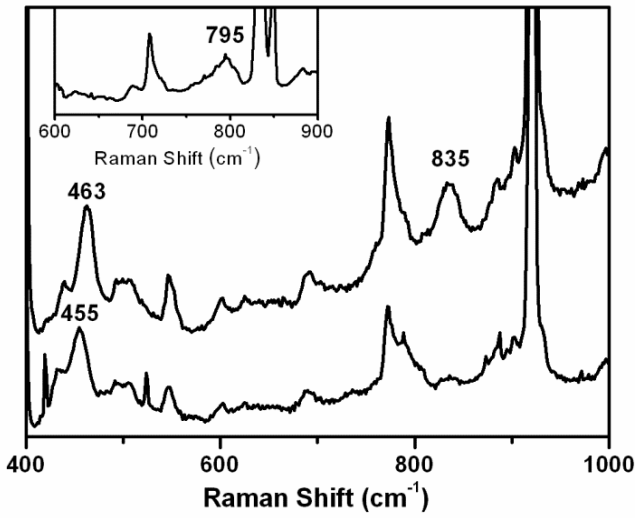

Figure 5. Resonance Raman spectra of **2A** in MeCN collected at 77 K with 413.1-nm excitation (100-mW power). Top: ^{16}O-labeled **2A**; bottom: ^{18}O-labeled **2A**. Inset: ^{18}O-labeled **2A** spectrum obtained in CD_3CN to unmask the downshifted ^{18}O vibration.

Because both **1A** and **2A** are able to activate H_2O_2 to form high-valent intermediates, the *pKa*'s of the precursors of the complexes with high-valent diiron cores have been investigated to determine the protonation states under different conditions Titrations of **2A** and **2B** in MeCN solution with small aliquots of a 3-bromopyridine reveal changes that can be monitored spectrophotometrically. Spectral data show that both **2A** and **2B** cleanly convert to **1A** and **1B** respectively with an increase in the concentration of 3-bromopyridine (Figure 6, showing the transformation from **2A** to **1A**, which is representative for both). A plot of A(550 nm) *vs.* concentration of 3-bromopyridine displayed in the inset of Figure 6 shows the p*K*a of **2A** to be at least 1 p*K*a unit higher than that of 3-bromopyridine (p*K*a = 2.84 in H_2O). On the other hand, the p*K*a of **2B** is comparable to that of 3-bromopyridine and thus about 1 p*K*a unit lower than that of **2A**, consistent with having less electron-donating pyridine donors. The difference in p*K*a between the diferric complexes supported by ligands **A** and **B** appears to be important. While diiron(III) complexes of other TPA-based ligands can be converted into $Fe^{III}Fe^{IV}(\mu\text{-}O)_2$ derivatives by treatment with H_2O_2,[7c,d] thus far only **2A** reacts with stoichiometric H_2O_2 to afford a high yield of **4A**. This outcome is presumably due to the presence of three electron donating substituents on each pyridine, which increase the basicity of ligand **A** to provide enough electron density to stabilize the diiron(IV) centers.

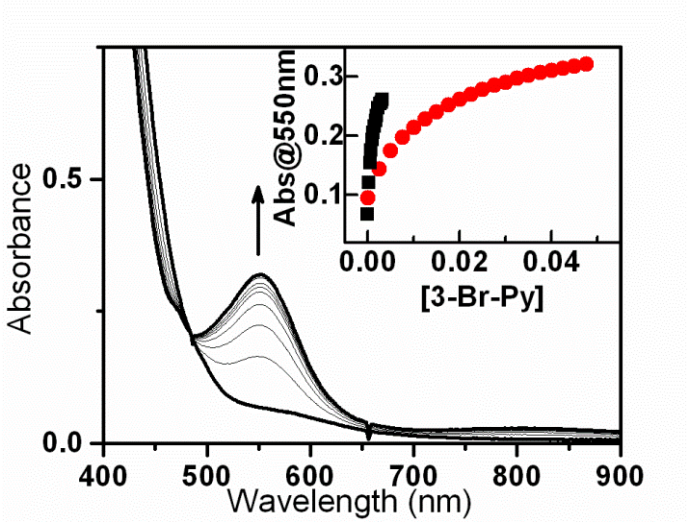

Figure 6. Titration of a 0.3-mM solution of **2A** in MeCN with 3-bromopyridine to form its conjugate base **1A** (λ_{max} 550 nm, ε_M ~900). Inset: Formation of **1A** (red circles) and **1B** (black squares) by the increase of the 550 nm band upon titration of **2A** and **2B** with 3-bromopyridine.

*Structural Characterization of **4A** and **3A***

Complex **4A** can be obtained by its one-step synthesis from the reaction of **2A** with one equivalent of 70% H_2O_2 at -40°C and exhibits a red color that results from the presence of electronic spectral features at λ_{max} 485 nm (ε_M 9,800 $M^{-1}cm^{-1}$) and 875 nm (ε_M 2,200 $M^{-1}cm^{-1}$). Its high yield of 85% has allowed diffraction-quality crystals of **4A** to be obtained. Crystallization of **4A** was achieved in a 3-step process by reacting 21 mg **2A** with one equivalent each of H_2O_2 and 3-bromopyridine in 2 mL butyronitrile at -40°C for 20 minutes to generate a dark red solution, followed by cooling to -80°C, and then layering with 1 mL diethyl ether. The dark red solution of **4A** persisted for weeks at -80°C and afforded dark red crystals in the shape of blocks, which were stable for months in the mother liquor at -80°C. At temperatures above -80°C and in the presence of the mother liquor, the dark red blocks lost crystallinity and quickly decayed to a green species that is likely the 1-e^- reduced species, **3A**. To obtain a structure of **4A**, a slide containing the dark red crystals was precooled with liquid N_2, and a suitable crystal was mounted quickly on an X-ray diffractometer. The time the crystal was not on the liquid nitrogen cooled slide or in the cold stream of the cryostat was minimized to slow solvent loss and preserve crystallinity.

The crystal diffracted to a resolution of 1.1 Å and was solved using direct methods (Figure 7).

Along with one-half of two molecules of interest (both located on inversion centers), 4 perchlorate counter ions and 5.5 butyronitrile molecules were found in the asymmetric unit. The loss of long-range order above -80°C was likely due to solvent loss rather than the decay of **4A**. The solvent molecules, along with the counter ions, create pockets that shield the tetra-cationic iron complexes from neighboring cations and give rise to a crystalline solid. After the data collection, the single crystal was transferred from the diffractometer to a microscope where it was observed to decay to a green solid, most likely the one-electron reduced **3A**. A separate batch of crystals, washed with diethyl ether at -80°C and then dissolved in acetonitrile at -40°C, afforded a solution that exhibited the characteristic electronic absorption and ESI-MS spectra of **4A**. The bond distances obtained from the diffraction analysis reported here are in good agreement with previously published EXAFS data;[7g] however the higher resolution of the crystal structure allowed differentiation between bonds not resolvable in the EXAFS experiment. Relevant bond distances comparing diiron complexes in different protonation and oxidation states are listed in Table 2 and discussed below.

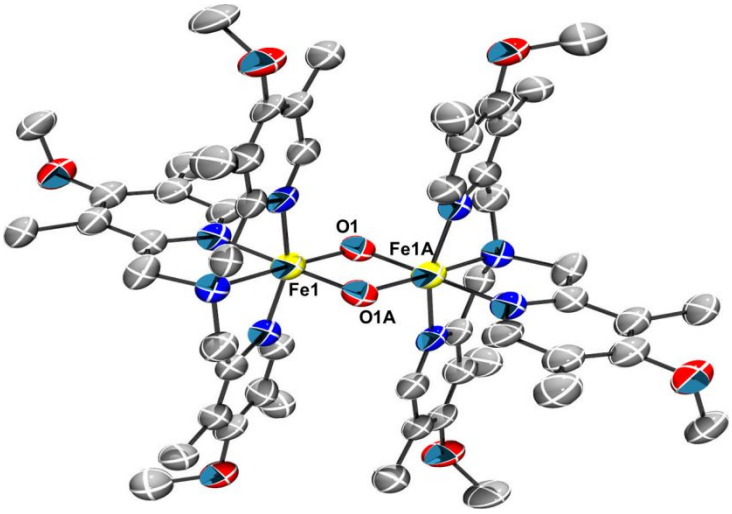

Figure 7. Structure of the tetracation of **4A** ($[(TPA^*)_2Fe^{IV}_2(\mu\text{-}O)_2]^{4+}$) with thermal ellipsoids drawn to the 50% probability level. Perchlorate counterions, butyronitrile solvent molecules and H-atoms were removed for clarity. Atom colors: carbon, gray; oxygen, red; nitrogen, blue; iron, yellow. An inversion center is present at the center of the Fe_2O_2 core of **4A**, making one half of the molecule unique. For a list of selected bond distances (Å) and angles (°) for **4A** and related structures, see Table 2.

For comparison, the crystal structure of **3A** has also been solved (Figure S1) from a diffraction-quality crystal obtained from butyronitrile/diethyl ether at -80°C. The green crystals of **3A** (λ_{max} 620 nm, ε ~ 6,000 $M^{-1}cm^{-1}$) are also susceptible to solvent loss, although to a lesser degree than **4A**, with one molecule of butyronitrile incorporated into the asymmetric unit. Nevertheless, mounting the crystal of **3A** onto the diffractometer required a cold mount, as described above for **4A** to maintain the crystallinity. As can be seen in Figures 7 and S1, **4A** and **3A** have nearly identical centrosymmetric structures. The inversion center observed for **3A** does not arise from crystallographic disorder of the iron(IV) and iron(III) centers but derives from the previously established valence-delocalized nature of the $[Fe^{III}Fe^{IV}(\mu\text{-}O)_2]^{3+}$ core, which arises from a novel double exchange mechanism.[7c] However, the differences in diiron oxidation state are manifested by changes in the iron-ligand bond distances from **3A** to **4A**. The $Fe–N_{ave}$ distance contracts by nearly 0.03 Å from 1.995(13) Å in **3A** to 1.969(8) Å in **4A**, but the Fe–O distances in the two complexes are within the uncertainty of the measurements (Table 2). Interestingly, the Fe•••Fe distance increases substantially from 2.596(1) Å in **3A** to 2.711(4) Å in **4A**. The contraction of the first coordination sphere and expansion of the Fe•••Fe distance give rise to a more distorted diamond core in **4A**, with the Fe–O–Fe angle deviating farther from the ideal 90° angle to 97.8° in **4A** versus 92.1° for **3A**. These crystallographic results solidify the initial structural characterization of **4A** by EXAFS, which revealed an Fe–O distance of 1.77 Å and an Fe•••Fe distance of 2.73 Å.[7g] Its surprisingly longer Fe•••Fe distance relative to the ~2.6-Å distance found for the one-electron reduced **3A** and **3B** may derive from two factors: a) the unequal Fe–O bond distances and the larger Fe–O–Fe angle found in the diamond core of **4A** and b) the greater repulsive force between two tetracationic point charges, relative to the smaller interaction between the 3.5+ charges on the Fe atoms in the valence-delocalized **3A**.

Not surprisingly, the Fe–O and Fe–N bond distances of the mixed-valent **3A** complex (Table 2) are found to be shorter by over 0.1 Å than the corresponding diferric species **1A** and **2A** due to the 0.5 increase in the oxidation state and a decrease in the spin states of the Fe atoms. Interestingly, the Fe–(μ-O)$_2$–Fe diamond core of **3A** is also found on an inversion center, with two distinct Fe–μ-O bond lengths, supporting the valence delocalized $Fe^{3.5+}$ oxidation state previously reported for **3B**.[7c,d] The Fe–O

lengths are 0.024 and 0.033 Å shorter and the average Fe–N bonds are shorter by over 0.030 Å for **3A** than corresponding values for **3B**. The contraction of the Fe–N bonds is rationalized by the more Lewis basic nature of ligand **A**. The shorter Fe–(μ-O) bonds of **3A** may be a result of the O–Fe–O angle being closer to the ideal 90°. Most notably, the Fe•••Fe distances for **3A** and **3B** are 2.596(1) Å and 2.683(1) Å, respectively. The shorter Fe•••Fe distance is mainly due to the contraction of the Fe–O bonds and the more acute Fe–O–Fe angle, which decreased from 94.1(1)° to 92.0(2)° from **3B** to **3A,** respectively.

An 8-mM frozen solution sample of **3A** analyzed by EXAFS corroborated the structural parameters found in its crystal structure. See Table 2 for a comparison of the crystallographic and EXAFS analysis results; more details can be found in Figure S2 and Table S4 in Supporting Information. Key EXAFS results are the two Fe–O scatterers found at 1.75 Å and assigned to the two oxo bridges as well as a prominent Fe•••Fe scatterer at 2.57 Å that strongly supports the persistence of the $[Fe^{III}Fe^{IV}(\mu\text{-}O)_2]^{3+}$ diamond core in solution. Both of these features are in reasonable agreement with the crystallographically determined distances reported herein (Table 2).

Thus the availability of solid-state structures for the **1A**-to-**4A** series provides an unprecedented opportunity to examine the metrical details of the Fe_2O_2 diamond core as the diiron oxidation state increases from Fe(III)Fe(III) through Fe(III)Fe(IV) to Fe(IV)Fe(IV). The obvious differences in iron oxidation states are also accompanied by spin state changes upon oxidation, starting from the S = 5/2 Fe(III) centers in **1A** and **2A**, progressing via a valence-delocalized S = 1/2 Fe(III)/S = 1 Fe(IV) center in **3A**, and finally to the S = 1 Fe(IV) centers in **4A**. The diamond core structure clearly has flexibility to adjust bond lengths and angles to accommodate the differences in charge, spin and protonation states. Notably, the Fe^{III}–μ-O_{oxo} EXAFS distance of 1.80 Å for **1A** is indistinguishable within the error of EXAFS analysis (0.02 Å) from the corresponding Fe–μ-O distances determined crystallographically for the higher-valent **3A** and **4A** complexes. Thus the Fe–μ-O_{oxo} bond distance essentially remains constant for the three structures with $Fe_2(\mu\text{-}O)_2$ cores in different iron oxidation states, leaving the Fe–N bonds to compensate for the changes in core charge.

Interestingly, the Fe•••Fe distances exhibit a relatively broad range of values, from 2.60 (**3A**) to 3.02 Å (**2A)**. The contraction of the Fe•••Fe distances upon oxidation parallels the decrease in the bond distances in the first coordination sphere except with **4A**. The tetracationic complexes **4A** and **2A** have the largest Fe–O–Fe angles at 98° and 101°, respectively, while the tricationic cores of **1A** and **3A** have angles much closer to 90°. The Lewis basicity of the ligands also has a dramatic effect on the Fe•••Fe distance as illustrated by a difference of almost 0.09 Å found between the Fe•••Fe distances of **3A** and **3B**. As there is about a 1 *pKa* unit difference in the precursor diferric compounds, the shorter Fe•••Fe distance of **3A** may result from the greater electron density donated by the more Lewis basic ligand **A** than ligand **B** to mitigate the +3.5 charge on each iron center, which decreases the repulsion between the two +3.5 point charges and allows for the angles of the $Fe_2(\mu\text{-}O)_2$ core to be closer to the ideal 90°. Finally, protonating the *μ*-oxo ligand in **1A** to a *μ*-hydroxo ligand in **2A** increases the Fe•••Fe distance by over 0.2 Å.

The relative accessibility of synthetic $[Fe_2(\mu\text{-}O)_2]$ diamond core complexes is demonstrated by our ability to form such high-valent species with various starting materials in different protonation and oxidation states and apply chemical or electrochemical methods. $[Fe^{III}Fe^{IV}(\mu\text{-}O)_2(5\text{-}Et_3TPA)_2]^{3+}$, the first structurally characterized example of such a diamond core complex,[7d] was reported in 1995 and obtained from the reaction of H_2O_2 with its diferric precursor $[Fe^{III}_2(\mu\text{-}O)(OH)(5\text{-}Et_3TPA)_2]^{3+}$.[7c] Subsequently, the higher valent $[Fe^{IV}_2(\mu\text{-}O)_2(TPA^*)_2]^{4+}$ complex could be obtained by 1-e oxidation of its $Fe^{III}Fe^{IV}$ analog.[7g] More recently, we found that the analogous higher valent $[Fe^{IV}_2(\mu\text{-}O)_2(Me_3NTB)_2]^{4+}$ complex could be formed using a more biomimetic reaction sequence, starting by exposing $[Fe^{II}_2(\mu\text{-}OH)_2(Me_3NTB)_2]^{2+}$ to O_2 forming the O_2 adduct and then followed by treatment with $Sc(OTf)_3$ to facilitate cleavage of the O–O bond and generate the bis(μ-oxo)diiron(IV) complex.[7j] (Me_3NTB is a tripodal ligand just like TPA* where the pyridines of the latter are replaced by *N*-methylbenzimidazoles.) In this report we demonstrate that the corresponding diferryl complex of TPA* can be formed by the reaction of the diferric precursor **2A** with stoichiometric H_2O_2 to generate **4A** in 85% yield. These reaction conditions have led to

the crystallization of $[Fe^{IV}_2(\mu\text{-}O)_2(TPA^*)_2]^{4+}$, affording the first crystal structure of a complex with an $Fe^{IV}_2(\mu\text{-}O)_2$ core.

The relative stability demonstrated for the $[Fe^{IV}_2(\mu\text{-}O)_2]$ core in these two examples may then be used to argue against the involvement of such structural motifs in biology for the hydroxylation of recalcitrant substrates as methane. It should be noted however that the iron(IV) centers found in the two synthetic complexes characterized with $[Fe^{IV}_2(\mu\text{-}O)_2]$ cores consist of S = 1 Fe^{IV}=O components, which have been shown for most cases to be less reactive than their S = 2 counterparts in biology. Whether the iron(IV) spin state plays such an important role in cleaving strong C–H bonds remains to be clarified, and this question is certainly worth exploring.

With respect to the question of whether sMMOH-**Q** has a diamond core structure as favored by its resonance Raman signature band[6d] and a very recently published study using NRVS (nuclear resonance vibrational spectroscopy)[6e] or an open-core structure as supported by recent EXAFS analyses,[6b,6c] we note that the synthetic $[Fe_2(\mu\text{-}O)_2]$ complexes we have studied demonstrate an interesting structural flexibility that can be related to their observed reactivity.[7g;9a,b,c] We have found that the diamond-core complexes characterized thus far are the least reactive of the series of complexes shown in Figure 8 with respect to their ability to oxidize 9,10-dihydroanthracene (DHA) at -80°C.[7g,h] with **4A** being an order of magnitude faster than **3A**. The mononuclear $[Fe^{IV}(O)(TPA^*)(NCMe)]^{2+}$ complex is yet another three orders of magnitude faster, demonstrating the even higher reactivity of the S = 1 terminal Fe^{IV}=O unit. However when the valence-delocalized $[Fe^{3.5}_2(\mu\text{-}O)_2]$ complex **3A** is treated with an equivalent of hydroxide, a valence-localized open-core adduct is formed (Scheme 4) that has an HAT rate 6.5 orders of magnitude faster than **4A**.[9a,b] The HAT rate becomes another 10-fold faster with the binding of fluoride (Scheme 4).[9c] Its high HAT reactivity stems from the unmasking of a terminal Fe^{IV}=O unit and its conversion into a high-spin Fe^{IV}=O unit upon F^- binding, both factors contributing to a much higher reactivity than found for a bridged oxo unit. Similar changes are observed for the hydroxide adduct, but hydrogen bonding of the O–H proton to the terminal Fe^{IV}=O unit decreases its HAT reactivity by approximately an order of magnitude. These proposed structural changes were corroborated by EXAFS analysis, which showed differences in the Fe•••Fe distances for

the two adducts, namely 3.56 Å for a nearly linear Fe–O–Fe unit in the fluoride adduct and 3.32 Å for the hydroxide adduct with an Fe–O–Fe angle of 130°.[9c]

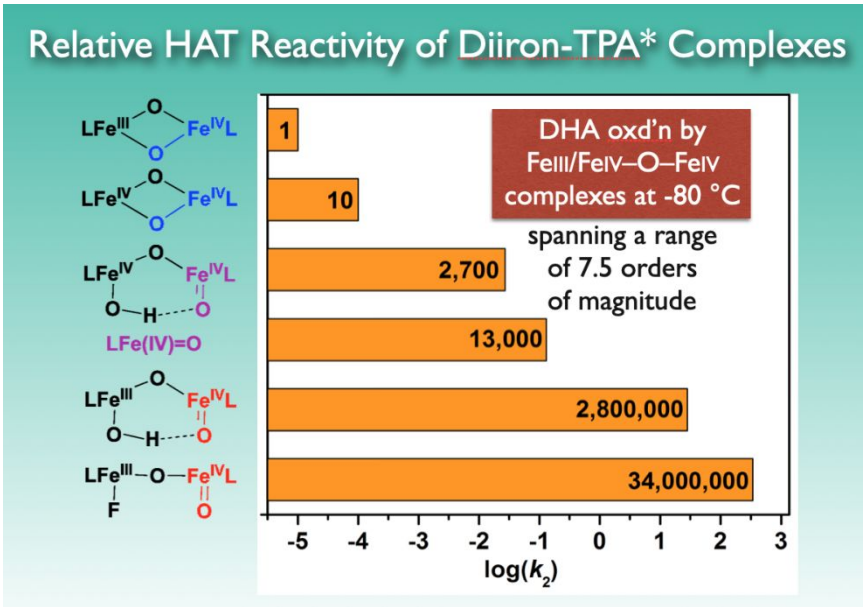

Figure 8. Relative rates for DHA oxidation at -80°C by a series of high-valent (μ-oxo)diiron(TPA*) complexes.[9a,b,c] Adapted from *Bull. Jpn. Soc. Coord. Chem*. 2013, **62**, 30 with permission from the Bulletin of the Japan Society of Coordination Chemistry.

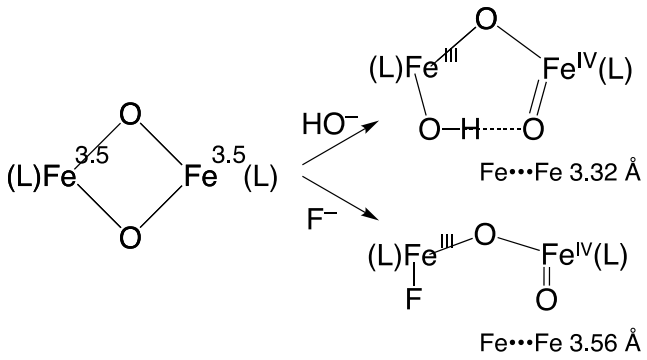

Scheme 4: Conversion of the valence-delocalized diamond core of **3A** into a valence-localized open X–Fe^{III}–O–Fe^{IV}=O core upon binding of OH^- or F^- to the Fe^{III} site to generate a more highly reactive terminal *S* = 2 Fe^{IV}=O unit.[9b,9c]

The $M_2(\mu\text{-}O)_2$ diamond-core reactivity story has been recently extended to include later first-row transition metal centers. Hildebrandt, Driess, and Ray have described a series of $[M^{III}(\mu\text{-}O)_2(M^{III})']^{2+}$ complexes of β-diketiminate ligands,[9e] with NiFe, NiCo, NiNi

and CoCo centers that carry out both nucleophilic and electrophilic oxidations; within the context of this paper, we just focus on their reported electrophilic reactivity with CHD. As listed in Table 3, these complexes exhibit a range of rates spanning two orders of magnitude, from 10^{-4} to 10^{-2} $M^{-1}s^{-1}$ at -60°C, many of which are more reactive than the corresponding high-valent diiron diamond core complexes described in this paper. Even more significant is the recent work of Wang and coworkers who have synthesized and characterized the $[Co^{III}Co^{IV}(\mu\text{-}O)_2(TPA)_2]^{3+}$ complex.[9f] Their EXAFS analysis of this complex has revealed a Co•••Co distance of 2.78 Å that is somewhat longer than the distances found crystallographically for its $Fe^{III}Fe^{IV}$ counterparts, 2.683(1) Å for the 5-Et_3TPA complex[7d] and 2.596(2) Å for the TPA* complex (reported in this paper). Most interestingly, the $Co^{III}Co^{IV}$ complex oxidizes DHA with k_2 = 1.5 $M^{-1}s^{-1}$ at -60°C, which is about 4 orders of magnitude more reactive than the related $[Fe^{III}Fe^{IV}(\mu\text{-}O)_2(TPA^*)_2]^{3+}$ complex after correcting for the temperature difference. This observation makes the $[Co^{III}Co^{IV}(\mu\text{-}O)_2(TPA)_2]^{3+}$ complex the most reactive in this series of diamond core complexes described to date and bodes well for more interesting oxidative chemistry to come.

Table 3. Related oxo-bridged dimetal complexes of interest

Complex	M•••M' distance (Å)[a]	k_2 for oxd'n in $M^{-1}s^{-1}$ [b]	refs
$[Fe^{III}Fe^{IV}(\mu\text{-}O)_2(5\text{-}Et_3\ TPA)_2]^{3+}$	2.683(1)	$5x10^{-4}$, -30°C, MeCN	7g
$[Fe^{III}Fe^{IV}(\mu\text{-}O)_2(TPA^*)_2]^{3+}$	2.596(2) (this work)	$1x10^{-5}$, -80°C [$1.6x10^{-4}$, -40°C] in 3:1 CH_2Cl_2/MeCN $4x10^{-5}$, -30°C, MeCN	9a 7h
$[Fe^{IV}_2(\mu\text{-}O)_2(TPA^*)_2]^{4+}$	2.711(4) (this work)	$1x10^{-4}$, -80°C [$1.6x10^{-3}$, -40°C] in 3:1 CH_2Cl_2/MeCN	9a
$[Fe^{IV}(O)(TPA^*)(NCMe)]^{2+}$	–	28, -80°C [~450, -40°C] in 3:1 CH_2Cl_2/MeCN	9a
$[Fe^{IV}_2(\mu\text{-}O)_2(Me_3NTB)_2]^{4+}$	*2.70*	*$7x10^{-4}$, -40°C, MeCN*	7j
$[Fe^{IV}(O)(Me_3NTB)(NCMe)]^{2+}$	–	*$9.4x10^{2}$, -40°C, MeCN*	7j
$[Co^{III}Co^{III}(L)_2]^{2+}$, L = β-ketimidate	2.6715(5)	*$6x10^{-3}$, -65°C, toluene*	9e
$[Co^{III}Ni^{III}(L)_2]^{2+}$, L = β-ketimidate	*2.72* (Co edge) *2.78* (Ni edge)	*$3.4x10^{-2}$, -65°C, toluene*	9e
$Ni^{III}Ni^{III}(L)_2]^{2+}$, L = β-ketimidate		*$2x10^{-2}$, -65°C, toluene*	9e
$[Cu^{III}Ni^{III}(L)_2]^{2+}$, L = β-ketimidate	*2.81* (at Cu and Ni edges)	*$5x10^{-4}$, -65°C, toluene*	9e
$[Co^{III}Co^{IV}(\mu\text{-}O)_2(TPA)_2]^{3+}$	*2.78*	*1.5, -60°C, MeCN*	9f

[a] M•••M' distances obtained by crystallography are shown in plain text, while those derived from EXAFS analysis are listed in italics.

[b] DHA oxidation rates are shown in plain text, while those for CHD oxidation are shown in italics. Values at -40°C shown in square brackets are extrapolated from -80°C by doubling the value every 10°C.

Acknowledgments

We are grateful to the U. S. National Institutes of Health for support of our work via grants R01 GM-38767 and R35 GM-131721 to L. Q. XAS data were collected on beamline X3B at the National Synchrotron Radiation Light Source, which is supported by the U.S. Department of Energy under Contract No. DE-AC02-98CH10886. Use of beamline X3B was made possible by the Center for Synchrotron Biosciences grant, P30-EB-00998, from the National Institute of Biomedical Imaging and Bioengineering.

Dedicated to Prof. John D. Lipscomb for his friendship and his brilliant career in studying methane monooxygenase and other nonheme iron oxygenases.

References

1. a) A. J. Jasniewski and L. Que, Jr., *Chem. Rev*. 2018, **118**, 2554;
   b) C. E. Tinberg and S. J. Lippard, *Acc. Chem. Res*. 2011, **44**, 280;
   c) R. Banerjee, J. C. Jones, J. D. Lipscomb, *Annu. Rev. Biochem*. 2019, **88**, 409.

2. sMMOH crystal structures:
   a) A. C. Rosenzweig, C. A. Frederick, S. J. Lippard, and P. Nordlund, *Nature* 1993, **366**, 537;
   b) A. C. Rosenzweig, and S. J. Lippard, *Acc. Chem. Res.* 1994, **27**, 229;
   c) V. Srinivas, R. Banerjee, H. Lebrette, J. C. Jones, O. Aurelius, I.-S. Kim, C. C. Pham, S. Gul, K. D. Sutherlin, K. D., A. Bhowmick, J. John, E. Bozkurt, T. Fransson, P. Aller, A. Butryn, I. Bogacz, P. Simon, S. Keable, A. Britz, K. Tono, K. S. Kim, S.-Y. Park, S. J. Lee, J. Park, R. Alonso-Mori, F. D. Fuller, A. Batyuk, A. S. Brewster, U. Bergmann, N. K. Sauter, A. M. Orville, V. K. Yachandra, J. Yano, J. D. Lipscomb, J. Kern, and M. Högbom, *J. Am. Chem. Soc.* 2020, **142**, 14249.

3. Early studies of sMMOH intermediates:
   a) B. G. Fox, M. P. Hendrich, K. K. Surerus, K. K. Andersson, W. A. Froland, J. D. Lipscomb, E. Münck, *J. Am. Chem. Soc*. 1993, **115**, 3688;
   b) S. K. Lee, B. G. Fox, W. A. Froland, J. D. Lipscomb, and E. Münck, *J. Am. Chem. Soc.* 1993, **115**, 6450;
   c) S. K. Lee, J. C. Nesheim, and J. D. Lipscomb, *J. Biol. Chem.* 1993, **268**, 21569;
   d) K. E. Liu, D. Wang, B. H. Huynh, D. E. Edmondson, A. Salifoglou, and S. J. Lippard, *J. Am. Chem. Soc*. 1994, **116**, 7465;
   e) K. E. Liu, A. M. Valentine, D. Wang, B. H. Huynh, D. E. Edmondson, A. Salifoglou, and S. J. Lippard, *J. Am. Chem. Soc.* 1995, **117**, 10174.

4. Synthetic diferric-peroxo complexes not crystallographically characterized:
   a) Y. Dong, Y. S. Ménage, B. A. Brennan, T. E. Elgren, H. G. Jang, L. L. Pearce, L. Que, Jr., *J. Am. Chem*. *Soc*. 1993, **115**, 1851;
   b) N. Kitajima, N. Tamura, H. Amagai, H. Fukui, Y. Moro-oka, Y. Mizutani, T. Kitagawa, R. Mathur, K. Heerwegh, C. A. Reed, C. R. Randall, L. Que, Jr., K. Tatsumi, *J. Am. Chem. Soc.* 1994, **116**, 9071;
   c) Y. Hayashi, T. Kayatani, H. Sugimoto, M. Suzuki, K. Inomata, A. Uehara, Y. Mizutani, T. Kitagawa, Y. Maeda, *J. Am. Chem. Soc.* 1995, **117**, 11220;
   d) Y. Dong, Y. Zang, L. Shu, E. C. Wilkinson, L. Que, Jr., K. Kauffmann, E. Münck, *J. Am. Chem. Soc*. 1997, **119**, 12683;
   e) J. R. Hagadorn, L. Que, Jr., W. B. Tolman, *J. Am. Chem. Soc*. 1998, **120**, 13531;
   f) D. Lee, J. DuBois, D. Petasis, M. P. Hendrich, C. Krebs, B. H. Huynh, S. J. Lippard, *J. Am. Chem. Soc*. 1999, **121**, 9893;
   g) M. Kodera, M. Itoh, K. Kano, T. Funabiki, M. Reglier, *Angew. Chem. Int. Ed*. 2005, **44**,

7104;
h) M. Kodera & K. Kano, *Bull. Chem. Soc. Jpn*. 2007, **80**, 662;
i) A. T. Fiedler, X. Shan, M. P. Mehn, J. Kaizer, S. Torelli, J. R. Frisch, M. Kodera, L. Que, Jr., *J. Phys. Chem. A* 2008, **112**, 13037;
j) M. A. Cranswick, K. K. Meier, X. Shan, A. Stubna, J. Kaizer, M. P. Mehn, E. Münck, L. Que, Jr., *Inorg. Chem*. 2012, **51**, 10417;
k) M. Kodera, Y. Kawahara, Y. Hitomi, T. Nomura, T. Ogura, Y. Kobayashi, *J. Am. Chem. Soc*. 2012, **134**, 13236;
l) M. Kodera, T. Tsuji, T. Yasunaga, Y. Kawahara, T. Hirano, Y. Hitomi, T. Nomura, T. Ogura, Y. Kobayashi, P. K. Sajith, Y. Shiota, K. Yoshizawa, *Chem. Sci.* 2014, **5**, 2282;
m) J. S. Pap, M. A. Cranswick, É. Balogh-Hergovich, G. Baráth, M. Giorgi, G. T. Rohde, J. Kaizer, G. Speier, L. Que, Jr., *Eur. J. Inorg. Chem*. 2013, 3858.

5. Crystallographically characterized diferric-peroxo model complexes:
a) Y. Dong, S. Yan, V. G. Young, Jr., L. Que, Jr., *Angew. Chem. Int. Ed.* 1996, **35**, 618;
b) K. Kim, S. J. Lippard, *J. Am. Chem. Soc.* 1996, **118**, 4914;
c) T. Ookubo, H. Sugimoto, T. Nagayama, H. Masuda, T. Sato, K. Tanaka, Y. Maeda, H. Okawa, Y. Hayashi, A. Uehara, M. Suzuki, *J. Am. Chem. Soc*. 1996, **118**, 701;
d) X. Zhang, H. Furutachi, S. Fujinami, S. Nagatomo, Y. Maeda, Y. Watanabe, T. Kitagawa, M. Suzuki, *J. Am. Chem. Soc*. 2005, **127**, 826.

6. Spectroscopic studies of sMMOH-**Q**:
a) L. Shu, J. C. Nesheim, K. Kauffmann, E. Münck, J. D. Lipscomb, L. Que, Jr., *Science* 1997, **275**, 515;
b) R. G. Castillo, R. Banerjee, C. J. Allpress, G. T. Rohde, E. Bill, L. Que, Jr., J. D. Lipscomb, and S. DeBeer, *J. Am. Chem. Soc.* 2017, **139**, 18024;
c) G. Cutsail III, R. Banerjee, A. Zhou, L. Que, Jr., J. D. Lipscomb, and S. DeBeer, *J. Am. Chem. Soc*. 2018, **140**, 16807;
d) R. Banerjee, Y. Proshlyakov, J. D. Lipscomb, D. A. Proshlyakov, *Nature* 2015, **518**, 431;
e) A. B. Jacobs, R. Banerjee, D. E. Deweese, A. Braun, J. T. Babicz, Jr., L. B. Gee, K. D. Sutherlin, L. H. Böttger, Y. Yoda, M. Saito, S. Kitao, Y. Kobayashi, M. Seto, K. Tamasaku, J. D. Lipscomb, K. Park, E. I. Solomon, *J. Am. Chem. Soc*. 2021, 143, in press, DOI: 10.1021/jacs1c05436.

7. Properties of synthetic diiron diamond core complexes related to sMMOH-**Q**:
a) L. Que, Jr. and W. B. Tolman, *Angew. Chem. Int. Ed.* 2002, **41**, 1114;
b) Y. Zang, Y. Dong, L. Que, Jr. K. Kauffmann, E. Münck, *J. Am. Chem. Soc*. 1995, **117**, 1169;
c) Y. Dong, H. Fujii, M. P. Hendrich, R. A. Leising, G. Pan, C. R. Randall, E. C. Wilkinson, Y. Zang, L. Que, Jr., B. G. Fox, K. Kauffmann, E. Münck, *J. Am. Chem. Soc.* 1995, **117**, 2778;
d) H.-F. Hsu, Y. Dong, L. Shu, V. G., Young, Jr., L. Que, Jr., *J. Am. Chem. Soc*. 1999, **121**, 5230;
e) H. Zheng, Y. Zang, Y. Dong, V. G. Young, Jr., L. Que, Jr., *J. Am. Chem. Soc.* 1999,

121, 2226;
f) L. H. Do, G. Xue, L. Que, Jr., S. J. Lippard, *Inorg. Chem.* 2012, **51**, 2393;
g) G. Xue, D. Wang, R. De Hont, A. T. Fiedler, X. Shan, E. Münck, L. Que, Jr., *Proc. Nat. Acad. Sci.* USA 2007, **104**, 20713;
h) G. Xue, A. T. Fiedler, M. Martinho, E. Münck, L. Que, Jr., *Proc. Nat. Acad. Sci. USA* 2008, **105**, 20615;
i) S. A. Stoian, G. Xue, E. L. Bominaar, L. Que, Jr., E. Münck, *J. Am. Chem. Soc*. 2014, **136**, 1545;
j) S. Banerjee; A. Draksharapu, P. M. Crossland, R. Fan, Y. Guo, M. Swart, L. Que, Jr., *J. Am. Chem. Soc.* 2020, **142**, 4285.

8. Vibrational data
a) J. Sanders-Loehr, W. D. Wheeler, A. K. Shiemke, B. A. Averill, T. M. Loehr, *J. Am. Chem. Soc.* 1989, **111**, 8084;
b) E. C. Wilkinson, Y. Dong, Y. Zang, H. Fujii, R. Fraczkiewicz, R. S. Czernuszewicz, and L. Que, Jr., *J. Am. Chem. Soc.* 1998, **120***,* 955;
c) A. J. Skulan, M. A. Hanson, H.-f. Hsu, L. Que, Jr., E. I. Solomon, *J. Am. Chem. Soc*. 2003, **125**, 7344.

9. HAT Reactivity of **Q**-related models:
a) G. Xue, R. De Hont, E. Münck, L. Que, *Nature Chem*. 2010, **2**, 400;
b) G. Xue, A. Pokutsa, L. Que, Jr., *J. Am. Chem. Soc*. 2011, **133**, 16657;
c) G. Xue, C. Geng, S. Ye, A. T. Fiedler, F. Neese, L. Que, Jr., *Inorg. Chem*. 2013, **52**, 3976;
d) S. Kundu, F. F. Pfaff, E. Miceli, I. Zaharieva, C. Herwig, S. Yao, E. R. Farquhar, U. Kuhlmann, E. Bill, P. Hildebrandt, H. Dau, M. Driess, C. Limberg, and K. Ray, *Angew. Chem. Int. Ed*. 2013, **52**, 5622;
e) X. Engelmann, S. Yao, E. R. Farquhar, T. Szilvási, U. Kuhlmann, P. Hildebrandt, M. Driess, K. Ray, *Angew. Chem. Int. Ed*. 2017, **56**, 297;
f) Y. Li, S. Handunneththige, E. R. Farquhar, Y. Guo, M. R. Talipov, F. Li, D. Wang, *J. Am. Chem. Soc.* 2019, **141**, 20127.

10. G. N. George, I. J. Pickering, EXAFSPAK, Stanford Synchrotron Radiation Laboratory, Stanford Linear Accelerator Center, Stanford, California, 2000.